Nanoscale synthesis of ionic analogues of bilayer silicene with high carrier mobility

High Carrier Mobility in Ionic Analogues of Bilayer Silicene

Dmitry V. Averyanov,[1] Peitao Liu,[2] Ivan S. Sokolov,[1] Oleg E. Parfenov,[1] Igor A. Karateev,[1]
Domenico Di Sante,[3] Cesare Franchini,[2,4] Andrey M. Tokmachev,[1] and Vyacheslav G. Storchak[1*]

[1] National Research Center "Kurchatov Institute", Kurchatov Sq. 1, 123182 Moscow, Russia
[2] University of Vienna, Faculty of Physics and Center for Computational Materials Science, A-1090 Vienna, Austria
[3] Institut für Theoretische Physik und Astrophysik and Würzburg-Dresden Cluster of Excellence ct.qmat, Universität Würzburg, Am Hubland Campus Süd, Würzburg 97074, Germany
[4] Dipartimento di Fisica e Astronomia, Università di Bologna, 40127 Bologna, Italy

KEYWORDS: bilayer silicene, high carrier mobility, nanoscale material, Zintl anion, epitaxial film

ABSTRACT: Design of materials with special properties benefits from establishing deep structural and electronic analogies between emerging and existing materials. The Zintl anion $[Al_2Si_2]^{2-}$ is both isostructural and isoelectronic to bilayer silicene; it thus makes a promising building block to assemble electronic materials. Here, we show that nanoscale films of $SrAl_2Si_2$, a semimetal formed by alternating $[Al_2Si_2]$ and Sr layers, exhibit a high carrier mobility, exceeding 10,000 $cm^2 V^{-1} s^{-1}$. The dominant role of the anionic bilayers in the electronic structure and transport properties is established by band structure calculations. To synthesize monocrystalline epitaxial films of $SrAl_2Si_2$ with atomically sharp interfaces, a general two-step route involving a sacrificial 2D template is devised. A distinct advantage of the films is their natural integration with silicon technology. The results establish a platform for engineering layered ionic nanomaterials.

INTRODUCTION

Intrinsic high carrier mobility is a marker of unconventional electronic structures and properties, found in graphene[1] and other 2D materials,[2,3] 3D Dirac[4] and Weyl[5] semimetals. Elemental analogues of graphene, 2D-Xenes,[6] are natural candidates for high carrier mobility, realized in germanene derivatives[7] but predicted also for silicene,[8] a material bringing together graphene and silicon technologies. As in the case of graphene,[9] a transition from mono- to bilayer silicene may engender new functionalities. Carrier mobilities in mono- and bilayer silicenes are expected to be of the same order of magnitude[10] but bilayer silicene may also host chiral superconductivity,[11] intrinsic 2D magnetism,[12] valley- and spin-dependent quantum Hall states.[13] Fragments of bilayer silicene embedded into a matrix have been produced[14] but they are very challenging to experiment with.

Despite a significant progress in handling silicene materials to build up multi-stack structures[15] synthesis of usable bilayer silicene is not on the horizon. However, bilayer silicene may serve as a blueprint for other functional materials. The concept of *isoelectronicity* guides design and rationalization of emerging materials, covalent 2D layers[16] and ionic Zintl compounds[17] alike. In particular, Klemm's pseudo-atom approach,[18] *i.e.* correspondence between the structural behavior and the formal total electron charge of atoms, can be employed. For instance, the anionic Al^-, isoelectronic to Si^0, is considered as pseudo-silicon.[19] Extending this similarity, the Zintl anion $[Al_2Si_2]^{2-}$ formed by two $[AlSi]^-$ layers makes an ionic analogue of bilayer silicene.

This 2D anion is a part of various layered compounds MAl_2Si_2 (Chart 1). Magnetotransport studies of bulk $CaAl_2Si_2$[20] reveal high carrier mobility; band structure calculations and photoemission spectroscopy[20,21] suggest the emergence of nontrivial topological features below the Fermi energy. Detailed analysis indicates that the inner structure of the double-layer anions shapes the electronic properties of $CaAl_2Si_2$ – at the Fermi level, bands of $CaAl_2Si_2$ are very close to those of $[Al_2Si_2]^{2-}$.[22,23] It substantiates the analogy between isolated bilayer silicene and the $[Al_2Si_2]^{2-}$ layers in ionic compounds. The dominant role of covalent

bilayers constitutes a general pattern illustrated by $EuCd_2As_2$, a magnetic topological material isostructural to $CaAl_2Si_2$;[24,25] its charge transport is predicted to be confined to the $[Cd_2As_2]^{2-}$ bilayers spaced by insulating cationic sheets.[26]

The discoveries of advanced physical properties provide opportunities in materials science. If indeed the anionic layers determine the electronic structures of MAl_2Si_2 then these compounds would make *a family of materials* with high carrier mobility and possibly other unconventional properties. On the other hand, the studies of $CaAl_2Si_2$ and related materials have been limited to bulk samples whereas applications would probably require nanomaterials.[27] It would be especially advantageous if they were seamlessly integrated with a semiconductor technological platform like silicon. This is a very challenging task entailing development of unconventional synthetic routes[28] rather different from those employed in synthesis of bulk crystals.

Here, we establish MAl_2Si_2 as a family of materials with similar electronic structures and transport properties, dominated by their bilayer anions. Among these materials, $SrAl_2Si_2$ is identified as having a synthetic route to single crystalline epitaxial films, produced on silicon via a two-step procedure employing a 2D nucleating template. The films exhibit high carrier mobilities exceeding 10^4 cm^2 V^{-1} s^{-1}.

EXPERIMENTAL AND COMPUTATIONAL DETAILS

Synthesis. The templates and $SrAl_2Si_2$ films were synthesized in a Riber Compact 12 system for molecular beam epitaxy. The base pressure in the growth chamber did not exceed 10^{-10} Torr. The substrates were high-ohmic Si(111) wafers of 1 inch $\times$ 1 inch area with miscut angles less than 0.5˚. The substrate temperature T_{Si} was measured by a thermocouple and a PhotriX ML-AAPX/090 infrared pyrometer operating at a 0.9 μm wavelength. Natural surface oxide was removed from the substrate surface by heating at 950 ˚C. 4N Sr and 5N Al were supplied from Knudsen cell effusion sources. First, 5 monolayers of $SrSi_2$ were synthesized by deposition of Sr on the Si surface at T_{Si} = 500 ˚C. It required heating the Sr effusion cell to T_{Sr} = 240 ˚C producing a Sr flux of 10^{-8} Torr, according to a Bayard-Alpert ionization gauge fitted at the substrate site. Then, the Si substrate was heated to 540 ˚C and treated with a mix of Sr and Al – the Sr flux kept the same, while the Al flux was set to $1.6{\cdot}10^{-8}$ Torr (T_{Al} = 955 ˚C). The resulting $SrAl_2Si_2$ films were annealed at 610 ˚C for 1 hour. Then, the films were capped at room temperature with 200 nm of amorphous SiO_x.

Characterization. The atomic structure of the films was characterized both *in situ* and *ex situ* employing a combination of techniques. In the growth chamber, the surface layer was continuously monitored by a RHEED diffractometer equipped with the kSA 400 analytical RHEED system. The overall structure of the films was then determined by a Rigaku SmartLab 9 kW diffractometer operating at a wavelength 1.54056 Å (Cu $K_{\alpha 1}$). The microstructure of the films was probed by high-resolution electron microscopy. Cross-sections of the samples were prepared in the Helios NanoLab 600i dual beam system. A 2 μm Pt layer was deposited on top of the film; then, a 2 μm $\times$ 5 μm $\times$ 5 μm lamella was cut out by 30 keV Ga^+ ions; it was further thinned by 5 keV and cleaned by 2 keV Ga^+ ions. Scanning transmission electron microscopy (STEM) images were produced by a Titan 80-300 Cs probe corrected microscope employing the high-angle annular dark-field (HAADF) mode. The images were processed by the Digital Micrograph and Tecnai Imaging and Analysis software.

Transport properties of the films were determined by a Lake Shore 9709A measurement system. Four-terminal sensing measurements were carried out employing square samples with a lateral size about 5 mm. Electrical contacts to the films were fabricated by *ex situ* deposition of an Ag-Sn-Ga alloy. It melts around room temperature and demonstrates excellent adhesion properties. The quality of the contacts was tested by measuring I-V characteristic curves.

Band structure. Band structure calculations were carried out with the Vienna *Ab initio* Simulation Package (VASP)[29,30] employing the projector augmented-wave pseudopotentials[31,32] and the revised Perdew-Burke-Ernzerhof (PBEsol) exchange-correlation functional.[33] The calculations adopted a plane-wave cutoff of 500 eV and a Γ-centered 12×12×8 *k*-point grid. The threshold for forces in full geometry relaxation was 5 meV/Å while the total energy was converged to 10^{-6} eV between two consecutive iterations. Transport properties were computed with the BoltzTraP code.[34] They were converged using a very dense *k*-point grid (50×50×25), then interpolated onto a mesh 5 times as dense. Charge analysis was carried out using the Bader approach.[35]

RESULTS AND DISCUSSION

MAl_2Si_2 – a Family of Materials. The $CaAl_2Si_2$ structural pattern – double-layer anions sandwiched between triangular cationic lattices – has given rise to a class of materials comprising more than 100 compounds.[36] These materials are best known for their excellent *n*- and *p*-type thermoelectric properties[36] to which carrier mobility is particularly important. We are interested in the MAl_2Si_2 subset of this class and the general role of the $[Al_2Si_2]^{2-}$ anion. For a detailed study we examine 3 such compounds – $CaAl_2Si_2$, $SrAl_2Si_2$, and $BaAl_2Si_2$. Their cationic layers are all formed by alkaline earths suggesting their similarity. In experiments, however, $SrAl_2Si_2$ crystallizes into the

same structure as $CaAl_2Si_2$ but $BaAl_2Si_2$ prefers the $Pnma$ space group.

We calculated the electronic structures of the 3 MAl_2Si_2 compounds employing density functional theory (DFT). The layered crystal structure is assumed to be of the $CaAl_2Si_2$ type belonging to space group $P\bar{3}m1$ (No. 164). As expected, the optimized lattice parameters increase from $CaAl_2Si_2$ to $SrAl_2Si_2$ to $BaAl_2Si_2$. The intralayer parameters $a = b$ change slightly, from 4.13 Å to 4.18 Å to 4.23 Å whereas increase in c is more pronounced, from 7.00 Å to 7.35 Å to 7.70 Å. The changes in different lattice parameters are almost proportional: $\Delta c/\Delta a$ is about 7.4 for the $CaAl_2Si_2$/$SrAl_2Si_2$ pair and 7.2 for the $CaAl_2Si_2$/$BaAl_2Si_2$ pair.

Figure 1 presents band structures and density of states (DOS) for the 3 MAl_2Si_2 compounds. They are semimetals and share a very similar band structure characterized by a pseudogap separating filled states of dominant Si-*p* character and the bottom of conduction band primarily formed by M-*d* states and Al-*s*/*p* orbitals. Interestingly, volume expansion associated with the chemical substitution from Ca to Ba leads to a progressive closing of the pseudogap. The electronic structure of $CaAl_2Si_2$ is consistent with that reported in Refs. [20, 37]. The similar band topology in all the systems points at the leading role of the $[Al_2Si_2]^{2-}$ anions. This conclusion is reinforced by a separate calculation of a $CaAl_2Si_2$ analogue with $[Al_2Si_2]$ block neutralized by charge compensation (Ca replaced by two excess electrons) – the resulting electronic structure remains similar to that of $CaAl_2Si_2$.

However, the role of metal cations is not negligible; they are not just innocent electron donors. Our calculations agree with the findings of Alemany *et al.*[22] that the cations in MAl_2Si_2 are essential to stabilize the bilayer structure and do contribute to the DOS near the Fermi level. The structural role of cations is manifested by different ground-state polymorphs of $CaAl_2Si_2$ and $BaAl_2Si_2$. The Bader charge analysis finds that the M states are populated appreciably; the 2- charge of $[Al_2Si_2]$ is nominal only. The estimated Bader charges in $CaAl_2Si_2$ are +1.30, +1.68, and -2.33 for Ca, Al, and Si, respectively, resulting in a state with -1.3 charge for $[Al_2Si_2]$.

The similar electronic structures of MAl_2Si_2 can be expected to yield similar transport properties. We checked this conjecture by calculating semiclassical transport coefficients. The carrier concentrations n (Figure 2a) are about 10^{19} cm^{-3}; they increase strongly with the chemical potential μ, which is typical for semimetals. What is most important is that the $n(\mu)$ curves are rather similar for different MAl_2Si_2 compounds. The same applies to the μ-dependent mobility/relaxation time ratio (Figure 2b). Thus, the electronic structure calculations characterize MAl_2Si_2 as a family of closely related materials; the advantageous properties of $CaAl_2Si_2$ such as high carrier mobility are expected to extend to other MAl_2Si_2 compounds. As different MAl_2Si_2 share the electronic structure, we choose the compound to experiment with based on the availability of synthetic routes.

Synthesis. Synthesis of bulk compounds of the $CaAl_2Si_2$ type has been studied extensively[36] – single crystals can be produced by direct reaction between the constituent elements. This approach fails, however, in attempts to make epitaxial films[28] – the grown films are polycrystalline and not particularly suitable for studies of intrinsic transport properties.

An alternative approach has been proposed in Ref. [28]. In the case of MAl_2Si_2, it involves synthesis of MSi_2 films on Si(111) with their subsequent transformation into MAl_2Si_2 by reaction with Al. Splitting the synthesis into 2 steps overcomes the hurdle posed by the lattice mismatch problem. Both steps lead to epitaxial films because the main changes in the unit cell occur in the direction orthogonal to the substrate surface – the reactions are classified as one-dimensional.[28] As demonstrated above, $CaAl_2Si_2$, $SrAl_2Si_2$, and $BaAl_2Si_2$ bear strong similarities in terms of the electronic structure and transport properties; however, the compounds are far from being equivalent in terms of synthesis of their films. The reason is the differences in the structure of the MSi_2 intermediates. The layered $CaSi_2$ suffers from a complex stacking sequence, at variance with the simple structure of $CaAl_2Si_2$; $BaSi_2$ crystallizes into non-layered orthorhombic polymorph with tetrahedral $[Si_4]^{4-}$ anions. In contrast, epitaxial films of layered $SrSi_2$ on Si(111)[38] are structurally similar to $SrAl_2Si_2$ and thus can be employed as a reactive precursor.[39]

Synthesis of $SrAl_2Si_2$ via intermediate $SrSi_2$ is viable for ultrathin films but has a serious limitation as soon as we aim at a film of considerable thickness. Al, deposited on top of the $SrSi_2$/Si(111) film, should reach all silicene-like monolayers of $SrSi_2$ to transform them into $[Al_2Si_2]$ bilayers. As the film thickness increases, the diffusion of Al becomes progressively more hindered. To tackle the problem, we present here an alternative synthetic route. It relies upon a 2D nucleating template to stabilize epitaxial growth of the film by direct reaction between the elements.

In Ref. [28], a few monolayers of $EuAl_2Si_2$ were used as a template to produce thick films of $EuAl_2Si_2$. A similar approach for $SrAl_2Si_2$ would require 3 steps: (i) synthesis of a few monolayers of $SrSi_2$ on Si(111); (ii) transformation of $SrSi_2$ into $SrAl_2Si_2$ template by reaction with Al; (iii) growth of $SrAl_2Si_2$ bulk by co-deposition of Sr and Al. We, however, omit the second step and grow $SrAl_2Si_2$ directly on $SrSi_2$. $SrSi_2$/Si(111) has been previously used as a template to synthesize heterostructures.[40] In the present work, the role of $SrSi_2$ is to be a sacrificial template – in the process, it should

accommodate excessive Al atoms and transform into $SrAl_2Si_2$. Thus, the synthesis involves 3 chemical reactions:

$$Sr + 2Si = SrSi_2 \quad (1)$$

as the first step;

$$SrSi_2 + 2Al = SrAl_2Si_2, \quad (2)$$

$$Sr + 2Al + 2Si = SrAl_2Si_2 \quad (3)$$

as the second step. Silicon for reactions (1) and (3) is supplied from the Si substrate serving as a reactant; Si atoms drift to the surface via the well-known vacancy mechanism. Following this route, we synthesized films up to 400 nm thick.

Structural Characterization. The structural quality of the films is important for the measurement of intrinsic transport properties. Sample characterization can also assess the merits of the proposed synthetic route. We employed 3 different techniques. RHEED was used to control the film surface *in situ*. Figure 3a demonstrates well-formed reflexes characteristic of a $SrAl_2Si_2$ film. The distance between the streaks determines the lattice parameter *a* in the film as 4.20(3) Å, close to the bulk value *a* = 4.1834(2) Å[41] and to DFT predictions. RHEED provides information on the surface and adjacent layers of the film only; it does not probe the inner layers of the film. X-ray diffraction (XRD) is a complementary technique capable to study the overall film structure. Figure 3b presents a typical θ-2θ XRD scan for a $SrAl_2Si_2$ film. It confirms that the film is epitaxial, with the layers parallel to the surface. The estimated lattice parameter *c* = 7.4220(12) Å corresponds well to the bulk value of 7.4104(2) Å[41] and to our DFT data. The XRD scan does not detect any side products, like $SrSi_2$ or SrAlSi. A small inclusion of the excessive reactant Al can be minimized by tuning its flux.

High-resolution electron microscopy provides a close look at the atomic structure of the film. Figure 4a demonstrates cross-section of the layered make-up of $SrAl_2Si_2$ – $[Al_2Si_2]$ bilayers are separated by Sr layers. The structure (*cf.* the side view given by Chart 1) corresponds to the simplest AA stacking of monolayers, the lowest in energy among buckled bilayer silicenes.[10] Figures 4b,c demonstrate that both interfaces of the $SrAl_2Si_2$ film are atomically abrupt. It is particularly important that the $SrSi_2$ layer is absent – it confirms the sacrificial character of the 2D template. HAADF-STEM images do not detect any extended structures of the excessive Al – they coalesce into isolated chunks and do not affect transport properties of the films.

Magnetotransport in $SrAl_2Si_2$. The ultimate purpose of the synthesis of $SrAl_2Si_2$ nanoscale films is to observe some unconventional properties distinguishing this material. Magnetotransport studies provide a simple probe of the electronic structure at the Fermi level. We measured the longitudinal (R_{xx}) and transverse (R_{xy}) resistance of $SrAl_2Si_2$ films as a function of applied magnetic field at room temperature and at 2 K. The data, translated into magnetoconductance σ_{xx} and σ_{xy}, are given in Figure 5. The field dependence is not trivial, as expected for silicides which transport properties are usually described by more than one band.

To interpret the magnetotransport properties of $SrAl_2Si_2$ films we approximated the data by multiple bands. Conventionally, the two-band model – one band for electrons and one band for holes – is considered sufficient. Its simplified version has been used to determine carrier concentrations and mobilities in $CaAl_2Si_2$.[20] For $SrAl_2Si_2$, we found that the two-band model is a reasonable approximation to the transport data at room temperature (Figure 5a) but the low-temperature transport is described rather poorly (Figure 5b). We addressed the problem employing a more general approach, quantitative mobility spectrum analysis of magnetic-field-dependent Hall and resistivity measurements.[42] It turns out that the data fit well to a 4-band model comprising 2 electron and 2 hole bands (Figure 5b).

The analysis provides concentrations for different carriers. At both room and low temperature, the concentration of electrons slightly exceeds that of holes, in contrast to the results for bulk $CaAl_2Si_2$.[20] However, the absolute values ($10^{18} \div 10^{19}$ cm^{-3}) are similar in $SrAl_2Si_2$ and $CaAl_2Si_2$. In $SrAl_2Si_2$, the carrier mobility is strongly temperature-dependent but the mobility of holes remains higher than that of electrons, again in contrast to bulk $CaAl_2Si_2$. At low temperature, the mobility of holes and electrons in $SrAl_2Si_2$ reaches 13.050 and 6.600 $cm^2V^{-1}s^{-1}$, respectively. The electron mobilities at 2 K in $SrAl_2Si_2$ films and bulk $CaAl_2Si_2$[20] are rather close but the hole mobility in $SrAl_2Si_2$ is about 15 times higher than that in its Ca counterpart. This is not a result of using the 4-band model because the two-band model predicts high carrier mobilities in $SrAl_2Si_2$ as well. High carrier mobilities in nanostructured semimetals are difficult to achieve[43] which makes the result for epitaxial $SrAl_2Si_2$ films particularly attractive.

CONCLUSIONS

Two key ingredients in developing a new material are its design and engineering. Here, aiming at high carrier mobility, we designed a class of MAl_2Si_2 materials employing structural and electronic analogies between the $[Al_2Si_2]^{2-}$ anion and bilayer silicene. DFT calculations indicate that MAl_2Si_2 represent a family of compounds with similar electronic structure and chemical properties, marked by the leading role of the trigonal anionic $[Al_2Si_2]^{2-}$ block, which has long been suggested as

a fundamental structural building unit.[44] To engineer epitaxial films of $SrAl_2Si_2$, a representative of the MAl_2Si_2 class, we devised a two-step synthetic route. It relies upon a sacrificial 2D template and can be extended to other ternary materials such as magnetic $EuAl_2Si_2$ or various MAl_2Ge_2. It would be also interesting to synthesize and study ultrathin films of MAl_2Si_2 – their close analogues MSi_2 demonstrate a strong dependence of the electronic and magnetic structures on the film thickness[45] as well as layer-dependent electron transport.[46] The salient feature of the $SrAl_2Si_2$ films is a high mobility of both electron and hole carriers. This is particularly important in view of the thermoelectric performance of MAl_2Si_2 compounds.[47] $SrAl_2Si_2$ may well be the first thermoelectric material of the $CaAl_2Si_2$ structural type[36] to be made into a nanoscale material.

AUTHOR INFORMATION

Corresponding Author

* Email: vgstorchak9@gmail.com (Vyacheslav G. Storchak)

Author Contributions

All authors have given approval to the final version of the manuscript.

Notes

The authors declare no competing financial interest.

ACKNOWLEDGMENT

This work is supported by NRC “Kurchatov Institute” [No. 1055 (infrastructure)], the Russian Foundation for Basic Research [grant 19-07-00249 (structural characterization)], and the Russian Science Foundation [grants 20-79-10028 (synthesis) and 19-19-00009 (studies of electron transport)]. D.V.A. acknowledges support from the President’s scholarship [SP 1398.2019.5]. The measurements have been carried out using equipment of the resource centers of electrophysical, laboratory X-ray, and electron microscopy techniques at NRC “Kurchatov Institute”.

REFERENCES

(1) Geim, A. K.; Novoselov, K. S. The Rise of Graphene. *Nat. Mater.* **2007**, *6*, 183-191.

(2) Li, L.; Yang, F.; Ye, G. J.; Zhang, Z.; Zhu, Z.; Lou, W.; Zhou, X.; Li, L.; Watanabe, K.; Taniguchi, T.; Chang, K.; Wang, Y.; Chen, X. H.; Zhang, Y. Quantum Hall Effect in Black Phosphorus Two-Dimensional Electron System. *Nat. Nanotechnol.* **2016**, *11*, 593-597.

(3) Wu, J.; Yuan, H.; Meng, M.; Chen, C.; Sun, Y.; Chen, Z.; Dang, W.; Tan, C.; Liu, Y.; Yin, J.; Zhou, Y.; Huang, S.; Xu, H. Q.; Cui, Y.; Hwang, H. Y.; Liu, Z.; Chen, Y.; Yan, B.; Peng, H. High Electron Mobility and Quantum Oscillations in Non-Encapsulated Ultrathin Semiconducting Bi_2O_2Se. *Nat. Nanotechnol.* **2017**, *12*, 530-534.

(4) Liang, T.; Gibson, Q.; Ali, M. N.; Liu, M.; Cava, R. J.; Ong, N. P. Ultrahigh Mobility and Giant Magnetoresistance in the Dirac Semimetal Cd_3As_2. *Nat. Mater.* **2015**, *14*, 280-284.

(5) Shekhar, C.; Nayak, A. K.; Sun, Y.; Schmidt, M.; Nicklas, M.; Leermakers, I.; Zeitler, U.; Skourski, Y.; Wosnitza, J.; Liu, Z.; Chen, Y.; Schnelle, W.; Borrmann, H.; Grin, Y.; Felser, C.; Yan, B. Extremely Large Magnetoresistance and Ultrahigh Mobility in the Topological Weyl Semimetal Candidate NbP. *Nat. Phys.* **2015**, *11*, 645-649.

(6) Molle, A.; Goldberger, J.; Houssa, M.; Xu, Y.; Zhang, S.-C.; Akinwande, D. Buckled Two-Dimensional Xene Sheets. *Nat. Mater.* **2017**, *16*, 163-169.

(7) Parfenov, O. E.; Averyanov, D. V.; Tokmachev, A. M.; Sokolov, I. S.; Karateev, I. A.; Taldenkov, A. N.; Storchak, V. G. High-Mobility Carriers in Germanene Derivatives. *Adv. Funct. Mater.* **2020**, *30*, 1910643.

(8) Ni, Z.; Liu, Q.; Tang, K.; Zheng, J.; Zhou, J.; Qin, R.; Gao, Z.; Yu, D.; Lu, J. Tunable Bandgap in Silicene and Germanene. *Nano Lett.* **2012**, *12*, 113-118.

(9) Andrei, E. Y.; MacDonald, A. H. Graphene Bilayers with a Twist. *Nat. Mater.* **2020**, *19*, 1265-1275.

(10) Padilha, J. E.; Pontes, R. B. Free-Standing Bilayer Silicene: The Effect of Stacking Order on the Structural, Electronic, and Transport Properties. *J. Phys. Chem. C* **2015**, *119*, 3818-3825.

(11) Liu, F.; Liu, C.-C.; Wu, K.; Yang, F.; Yao, Y. *d+id’* Chiral Superconductivity in Bilayer Silicene. *Phys. Rev. Lett.* **2013**, *111*, 066804.

(12) Wang, X.; Wu, Z. Intrinsic Magnetism and Spontaneous Band Gap Opening in Bilayer Silicene and Germanene. *Phys. Chem. Chem. Phys.* **2017**, *19*, 2148-2152.

(13) Do, T.-N.; Gumbs, G.; Shih, P.-H.; Huang, D.; Lin, M.-F. Valley- and Spin-Dependent Quantum Hall States in Bilayer Silicene. *Phys. Rev. B* **2019**, *100*, 155403.

(14) Yaokawa, R.; Ohsuna, T.; Morishita, T.; Hayasaka, Y.; Spencer, M. J. S.; Nakano, H. Monolayer-to-Bilayer Transformation of Silicenes and Their Structural Analysis. *Nat. Commun.* **2016**, *7*, 10657.

(15) Martella, C.; Faraone, G.; Alam, M. H.; Taneja, D.; Tao, L.; Scavia, G.; Bonera, E.; Grazianetti, C.; Akinwande, D.; Molle, A. Disassembling Silicene from Native Substrate and Transferring onto an Arbitrary Target Substrate. *Adv. Funct. Mater.* **2020**, *30*, 2004546.

(16) Xia, F.; Wang, H.; Hwang, J. C. M.; Castro Neto, A. H.; Yang, L. Black Phosphorus and Its Isoelectronic Materials. *Nat. Rev. Phys.* **2019**, *1*, 306-317.

(17) Wilson, R. J.; Weigend, F.; Dehnen, S. The Arachno-Zintl Ion $(Sn_5Sb_3)^{3-}$ and the Effects of Element Composition on the Structures of Isoelectronic Clusters: Another Facet of the Pseudo-Element Concept. *Angew. Chemie Int. Ed.* **2020**, *59*, 14251-14255.

(18) Nesper, R. The Zintl-Klemm Concept – A Historical Survey. *Z. Anorg. Allg. Chem.* **2014**, *640*, 2639-2648.

(19) Vegas, A.; García-Baonza, V. Pseudoatoms and Preferred Skeletons in Crystals. *Acta Cryst. B* **2007**, *63*, 339-345.

(20) Su, H.; Shi, X.; Xia, W.; Wang, H.; Hanli, X.; Yu, Z.; Wang, X.; Zou, Z.; Yu, N.; Zhao, W.; Xu, G.; Guo, Y. Magnetotransport and *Ab Initio* Calculation Studies on the Layered Semimetal $CaAl_2Si_2$ Hosting Multiple Nontrivial Topological States. *Phys. Rev. B* **2020**, *101*, 205138.

(21) Deng, T.; Chen, C.; Su, H.; He, J.; Liang, A.; Cui, S.; Yang, H.; Wang, C.; Huang, K.; Jozwiak, C.; Bostwick, A.; Rotenberg, E.; Lu, D.; Hashimoto, M.; Yang, L.; Liu, Z.; Guo, Y.; Xu, G.; Liu, Z.; Chen, Y. Electronic Structure of the Si-Containing Topological Dirac Semimetal $CaAl_2Si_2$. *Phys. Rev. B* **2020**, *102*, 045106.

(22) Alemany, P.; Llunell, M.; Canadell, E. Roles of Cations, Electronegativity Difference, and Anionic Interlayer Interactions in the Metallic versus Nonmetallic Character of Zintl Phases Related to Arsenic. *J. Comput. Chem.* **2008**, *29*, 2144-2153.

(23) Semi, T. E. The Mechanism Behind the Calcium Aluminum Silicide Ternary Structural Preference and the Origin of its Semimetal Behavior. PhD Thesis, Colorado School of Mines, **2013**.

(24) Ma, J.-Z.; Nie, S. M.; Yi, C. J.; Jandke, J.; Shang, T.; Yao, M. Y.; Naamneh, M.; Yan, L. Q.; Sun, Y.; Chikina, A.; Strocov, V. N.; Medarde, M.; Song, M.; Xiong, Y.-M.; Xu, G.; Wulfhekel, W.; Mesot, J.; Reticcioli, M.; Franchini, C.; Mudry, C.; Müller, M.; Shi, Y. G.; Qian, T.; Ding, H.; Shi, M. Spin Fluctuation Induced Weyl Semimetal State in the Paramagnetic Phase of $EuCd_2As_2$. *Sci. Adv.* **2019**, *5*, eaaw4718.

(25) Ma, J.; Wang, H.; Nie, S.; Yi, C.; Xu, Y.; Li, H.; Jandke, J.; Wulfhekel, W.; Huang, Y.; West, D.; Richard, P.; Chikina, A.; Strocov, V. N.; Mesot, J.; Weng, H.; Zhang, S.; Shi, Y.; Qian, T.; Shi, M.; Ding, H. Emergence of Nontrivial Low-Energy Dirac Fermions in Antiferromagnetic $EuCd_2As_2$. *Adv. Mater.* **2020**, *32*, 1907565.

(26) Rahn, M. C.; Soh, J.-R.; Francoual, S.; Veiga, L. S. I.; Strempfer, J.; Mardegan, J.; Yan, D. Y.; Guo, Y. F.; Shi, Y. G.; Boothroyd, A. T. Coupling of Magnetic Order and Charge Transport in the Candidate Dirac Semimetal $EuCd_2As_2$. *Phys. Rev. B* **2018**, *97*, 214422.

(27) Liu, P.; Williams, J. R.; Cha, J. J. Topological Nanomaterials. *Nat. Rev. Mater.* **2019**, *4*, 479-496.

(28) Tokmachev, A. M.; Averyanov, D. V.; Karateev, I. A.; Sokolov, I. S.; Parfenov, O. E.; Storchak, V. G. Dimensionality Concept in Solid-State Reactions: A Way to Control Synthesis of Functional Materials at the Nanoscale. *Adv. Funct. Mater.* **2020**, *30*, 2002691.

(29) Kresse, G.; Hafner, J. *Ab Initio* Molecular Dynamics for Liquid Metals. *Phys. Rev. B* **1993**, *47*, 558-561.

(30) Kresse, G.; Furthmüller, J. Efficient Iterative Schemes for *Ab Initio* Total-Energy Calculations Using a Plane-Wave Basis Set. *Phys. Rev. B* **1996**, *54*, 11169-11186.

(31) Blöchl, P. E. Projector Augmented-Wave Method. *Phys. Rev. B* **1994**, *50*, 17953-17979.

(32) Kresse, G.; Joubert, D. From Ultrasoft Pseudopotentials to the Projector Augmented-Wave Method. *Phys. Rev. B* **1999**, *59*, 1758-1775.

(33) Perdew, J. P.; Ruzsinszky, A.; Csonka, G. I.; Vydrov, O. A.; Scuseria, G. E.; Constantin, L. A.; Zhou, X.; Burke, K. Restoring the Density-Gradient Expansion for Exchange in Solids and Surfaces. *Phys. Rev. Lett.* **2008**, *100*, 136406.

(34) Madsen, G. K. H.; Singh, D. J. BoltzTraP. A Code for Calculating Band-Structure Dependent Quantities. *Comp. Phys. Commun.* **2006**, *175*, 67-71.

(35) Henkelman, G.; Arnaldsson, A.; Jónsson, H. A Fast and Robust Algorithm for Bader Decomposition of Charge Density. *Comp. Mater. Sci.* **2006**, *36*, 354-360.

(36) Peng, W.; Chanakian, S.; Zevalkink, A. Crystal Chemistry and Thermoelectric Transport of Layered AM_2X_2 Compounds. *Inorg. Chem. Front.* **2018**, *5*, 1744-1759.

(37) Huang, G. Q. Electronic Structure and Transport Properties of Semimetal $CaAl_2Si_2$. *J. Phys.: Conf. Ser.* **2006**, *29*, 73-76.

(38) Tokmachev, A. M.; Averyanov, D. V.; Karateev, I. A.; Parfenov, O. E.; Vasiliev, A. L.; Yakunin, S. N.; Storchak, V. G. Topotactic Synthesis of the Overlooked Multilayer Silicene Intercalation Compound $SrSi_2$. *Nanoscale* **2016**, *8*, 16229-16235.

(39) Beekman, M.; Kauzlarich, S. M.; Doherty, L.; Nolas, G. S. Zintl Phases as Reactive Precursors for Synthesis of Novel Silicon and Germanium-Based Materials. *Materials* **2019**, *12*, 1139.

(40) Tokmachev, A. M.; Averyanov, D. V.; Karateev, I. A.; Parfenov, O. E.; Kondratev, O. A.; Taldenkov, A. N.; Storchak, V. G. Engineering of Magnetically Intercalated Silicene Compound: An Overlooked Polymorph of $EuSi_2$. *Adv. Funct. Mater.* **2017**, *27*, 1606603.

(41) Kauzlarich, S. M.; Condron, C. L.; Wassei, J. K.; Ikeda, T.; Snyder, G. J. Structure and High-Temperature Thermoelectric Properties of $SrAl_2Si_2$. *J. Solid State Chem.* **2009**, *182*, 240-245.

(42) Vurgaftman, I.; Meyer, J. R.; Hoffman, C. A.; Redfern, D.; Antoszewski, J.; Faraone, L.; Lindemuth, J. R. Improved Quantitative Mobility Spectrum Analysis for Hall Characterization. *J. Appl. Phys.* **1998**, *84*, 4966-4973.

(43) Zhang, C.; Ni, Z.; Zhang, J.; Yuan, X.; Liu, Y.; Zou, Y.; Liao, Z.; Du, Y.; Narayan, A.; Zhang, H.; Gu, T.; Zhu, X.; Pi, L.; Sanvito, S.; Han, X.; Zou, J.; Shi, Y.; Wan, X.; Savarsov, S. Y.; Xiu, F. Ultrahigh Conductivity in Weyl Semimetal NbAs Nanobelts. *Nat. Mater.* **2019**, *18*, 482-488.

(44) Burdett, J. K.; Miller, G. J. Fragment Formalism in Main-Group Solids: Applications to AlB_2, $CaAl_2Si_2$, $BaAl_4$, and Related Materials. *Chem. Mater.* **1990**, *2*, 12-26.

(45) Tokmachev, A. M.; Averyanov, D. V.; Parfenov, O. E.; Taldenkov, A. N.; Karateev, I. A.; Sokolov, I. S.; Kondratev, O. A.; Storchak, V. G. Emerging Two-Dimensional Ferromagnetism in Silicene Materials. *Nat. Commun.* **2018**, *9*, 1672.

(46) Parfenov, O. E.; Tokmachev, A. M.; Averyanov, D. V.; Karateev, I. A.; Sokolov, I. S.; Taldenkov, A. N.; Storchak, V. G. Layer-Controlled Laws of Electron Transport in Two-Dimensional Ferromagnets. *Mater. Today* **2019**, *29*, 20-25.

(47) Qin, Y.; Xiao, Y.; Zhao, L.-D. Carrier Mobility Does Matter for Enhancing Thermoelectric Performance. *APL Mater.* **2020**, *8*, 010901.

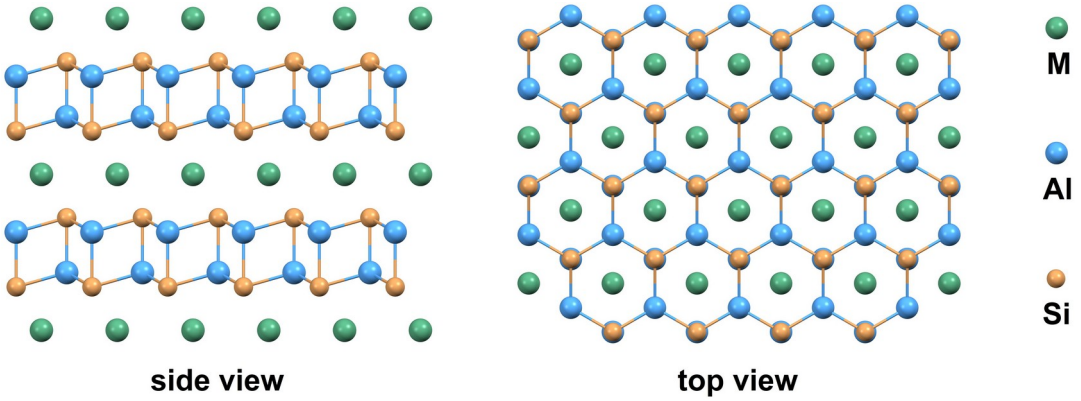

Chart 1. A ball-and-stick model of MAl_2Si_2 compounds. Side view demonstrates covalent $[Al_2Si_2]$ bilayers sandwiched between cationic layers. Top view shows that the M cation projections are to the centers of the hexagons forming the honeycomb structure of $[Al_2Si_2]$.

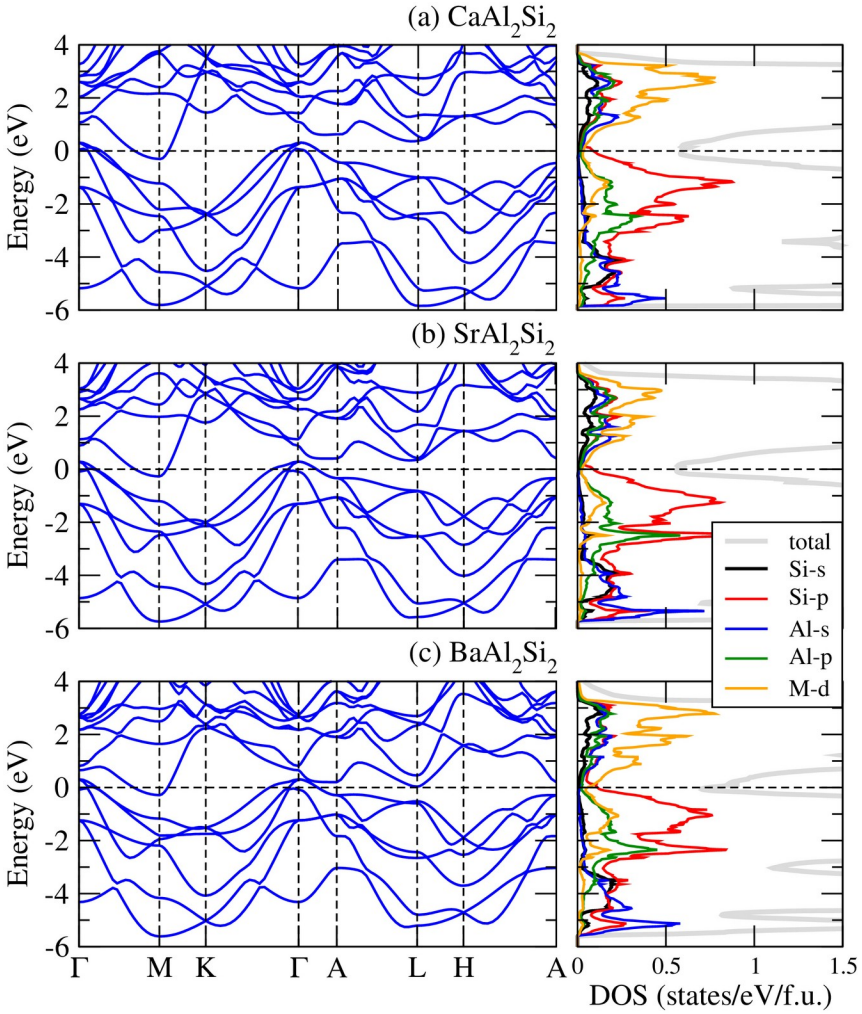

Figure 1. Band structures and DOS plots for (a) $CaAl_2Si_2$, (b) $SrAl_2Si_2$, and (c) $BaAl_2Si_2$.

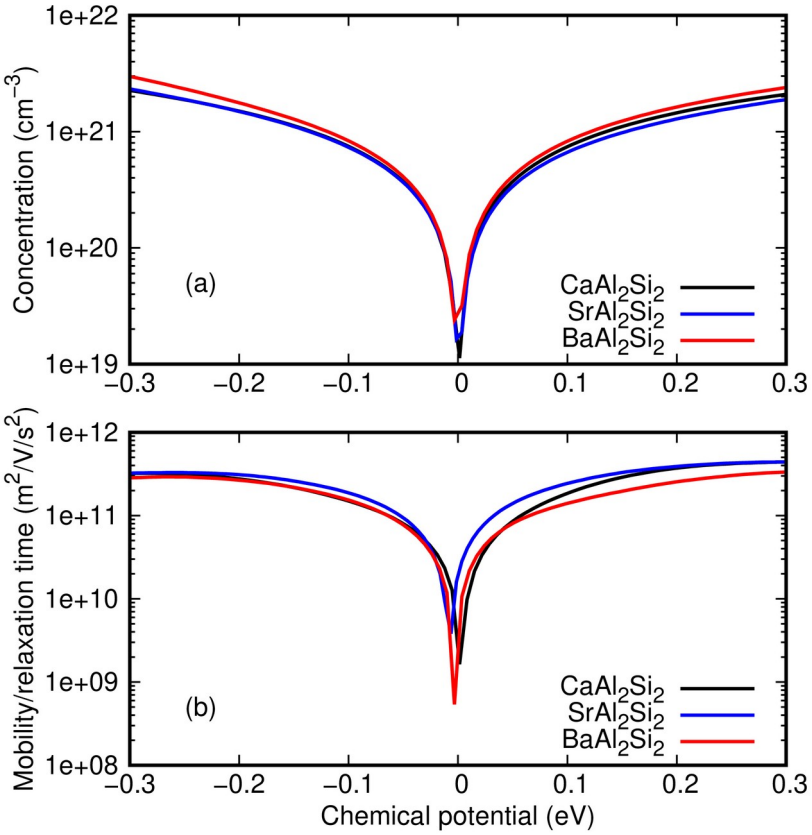

Figure 2. (a) Carrier concentration and (b) carrier mobility over relaxation time in MAl_2Si_2 (M = Ca, Sr, and Ba) as a function of chemical potential at 300 K.

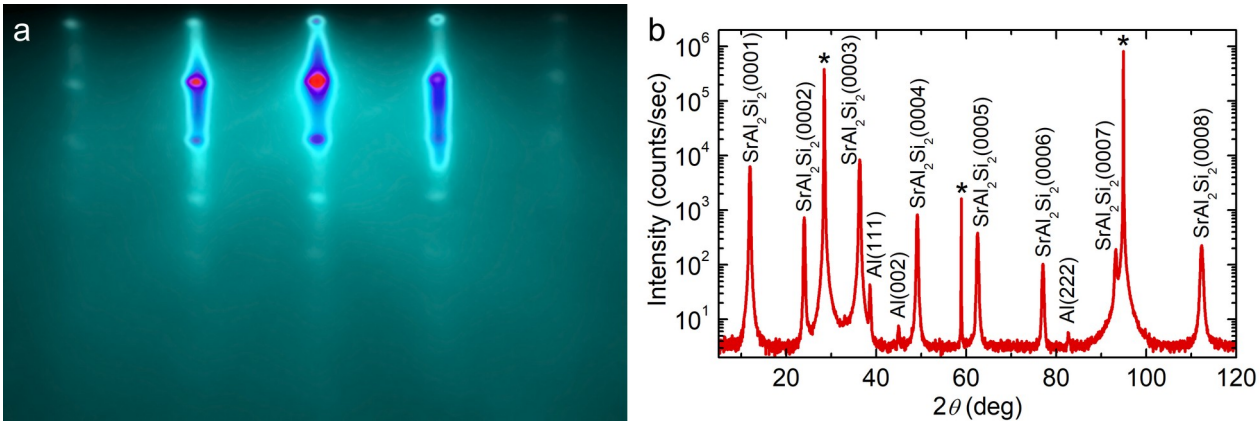

Figure 3. (a) A RHEED image of a $SrAl_2Si_2$ film (d = 70 nm) viewed along azimuth $[1\bar{1}0]$ of the substrate. (b) A θ-2θ diffraction scan for a film of $SrAl_2Si_2$ (d = 70 nm) on Si(111); asterisk denotes peaks from the substrate.

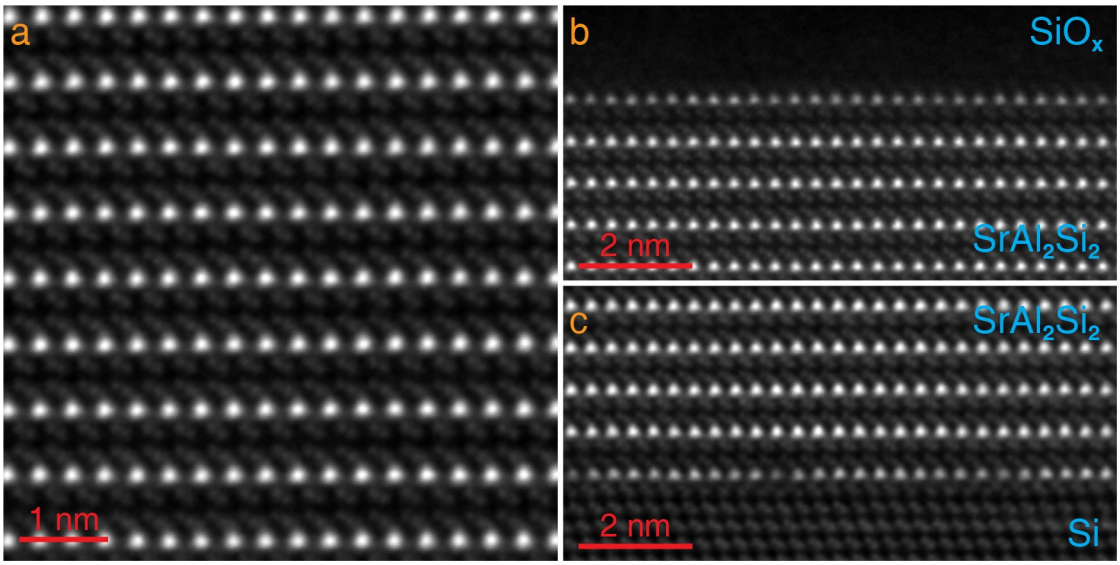

Figure 4. High-resolution HAADF-STEM images of $SiO_x/SrAl_2Si_2/Si(111)$: (a) the layered structure of $SrAl_2Si_2$, (b) $SiO_x/SrAl_2Si_2$ interface, and (c) $SrAl_2Si_2/Si(111)$ interface.

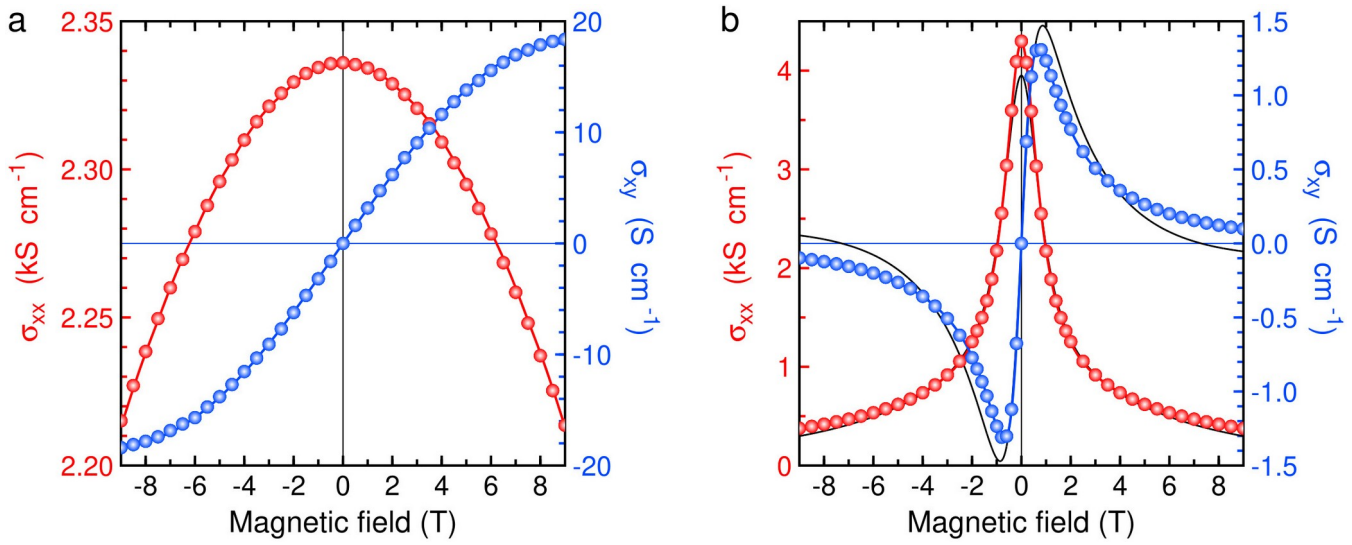

Figure 5. Longitudinal (red) and transverse (blue) magnetoconductance of $SrAl_2Si_2$ (d = 400 nm) at (a) 300 K and (b) 2 K. Dots show experimental data, solid lines provide their interpolation by a two-band model at 300 K and a 4-band model at 2 K; for comparison, an interpolation of the magnetotransport at 2 K by a two-band model is also provided (black).

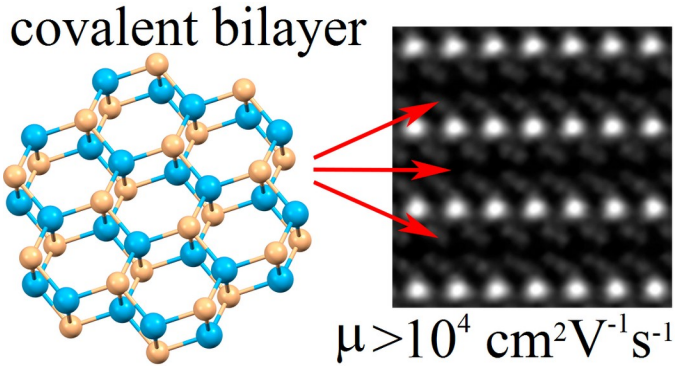

Table of Contents artwork